Electric Power Components and Systems

Advanced Simulation Model for Brushless DC Motor Drives

BYOUNG-KUK LEE [a] & MEHRDAD EHSANI [b]

[a] Korea Electrotechnology Research Institute, Power Electronics Group, Changwon, Korea

[b] Texas A&M University, Department of Electrical Engineering, College Station, Texas

PLEASE SCROLL DOWN FOR ARTICLE

Taylor & Francis
Taylor & Francis Group

Advanced Simulation Model for Brushless DC Motor Drives

BYOUNG-KUK LEE

Korea Electrotechnology Research Institute
Power Electronics Group
Changwon, Korea

MEHRDAD EHSANI

Texas A&M University
Department of Electrical Engineering
College Station, Texas

An advanced simulation model for brushless dc (BLDC) motor drives using Matlab is presented. In the developed model, the dynamic characteristics of speed and torque as well as voltages and currents of pwm inverter components can be effectively monitored and analyzed. Therefore, it can be expected that the developed simulation model can be an easy-to-design tool for the development of BLDC motor drives including control algorithms and topological variations with reduced computation time and memory size.

Keywords burshless dc motors, electric drive simulations, electric motor control

1. Introduction

Brushless dc (BLDC) motor drives are becoming widely used in various consumer and industrial systems, such as servo motor drives, home appliances, computer peripherals, and automotive applications [1–5]. Consequently, many machine design and control schemes have been developed to enhance the performance of BLDC motor drives [6–8]. In general, the overall system consists of three parts: (1) power conversion pwm inverters, (2) BLDC motor and load, and (3) speed, torque, and current controllers. Therefore, exact understanding of each part is a prerequisite for analysis and prediction of the overall system operation.

Before now, several simulation models have been proposed for the analysis of BLDC motor drives. These models are based on state-space equations, Fourier series, and the d-q axis model [9–12]. Even though the previous works made a great contribution to analysis of BLDC motor drives, to the best of our knowledge, no unified approach for modeling and analysis of the three parts of the drive has been proposed. In [11], the authors proposed a model by means of state array matrices to sim-

ulate the drive system along with the pwm inverter. However, in addition to its inherent complexity, detailed investigation of the inverter is not included in this work.

In this paper we propose a simulation model for an entire BLDC motor drive and its actual implementation. In this model the trapezoidal back EMF waveforms are modeled as a function of rotor position, so that position can be actively calculated according to the operating speeds. Moreover, the switching function concept is adopted to model the pwm inverter. This in turn results in obtaining the detailed voltage and current waveforms of the inverter and calculating the design parameters, such as average/rms ratings of components [13–17]. The developed model can produce a precise prediction of drive performance during transient as well as steady-state operation. Therefore, the mechanism of phase commutation and generation of torque ripple can be observed and analyzed in this model. In particular, the proposed model is made into several functional modular blocks, so that it can be easily extended to other ac motor applications with a little modification, such as the induction motor, the permanent magnet ac motor, and the synchronous reluctance motor.

Therefore, it can be expected that the developed simulation model can be an easy-to-design tool for the development of BLDC motor drives including control algorithms and topological variations with reduced computation time and memory size.

2. Analysis of BLDC Motor Drive System

Figure 1 shows the overall system configuration of the three-phase BLDC motor drive. The pwm inverter topology is a six-switch voltage-source configuration with constant dc-link voltage (V_d), which is identical with the induction motor drives and the permanent magnet ac motor drives. The analysis is based on the following assumption for simplification [12]:

1. The motor is not saturated.
2. Stator resistances of all the windings are equal, and self- and mutual inductances are constant.
3. Power semiconductor devices in the inverter are ideal.
4. Iron losses are negligible.

Among the above-mentioned assumptions, the iron loss can be approximated using empirical equations, and the dynamic characteristics of the switching devices need to be considered for the investigation of transient state behavior.
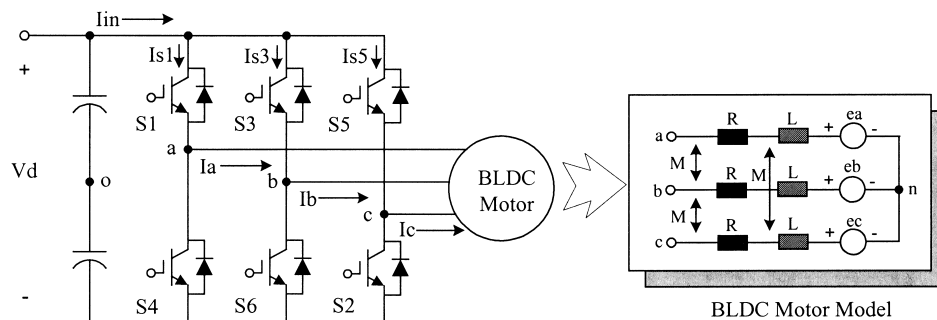

Figure 1. Configuration of BLDC motor drive system.

Under the above assumptions, a BLDC motor can be represented as

$$\begin{bmatrix} v_a \\ v_b \\ v_c \end{bmatrix} = \begin{bmatrix} R & 0 & 0 \\ 0 & R & 0 \\ 0 & 0 & R \end{bmatrix} \begin{bmatrix} i_a \\ i_b \\ i_c \end{bmatrix} + \begin{bmatrix} L-M & 0 & 0 \\ 0 & L-M & 0 \\ 0 & 0 & L-M \end{bmatrix} \frac{d}{dt} \begin{bmatrix} i_a \\ i_b \\ i_c \end{bmatrix} + \begin{bmatrix} e_a \\ e_b \\ e_c \end{bmatrix}, \quad (1)$$

where e_a, e_b, and e_c are trapezoidal back EMFs.

The electromagnetic torque is expressed as

$$T_e = T_L + J\frac{d\omega_r}{dt} + B\omega_r, \quad (2)$$

where T_L is load torque, J is inertia, and B is damping.

The pwm three-phase inverter operation can be divided into six modes according to the current conduction states as shown in Figure 2. The detailed switching states and conduction sequence are described in Figure 3.

The three phase currents are controlled to take a type of quasi-square waveform in order to synchronize with the trapezoidal back EMF to produce the constant torque. This task is performed by the speed/torque control loop in cooperation with the rotor position sensor and hysteresis current controller as shown in Figure 4.
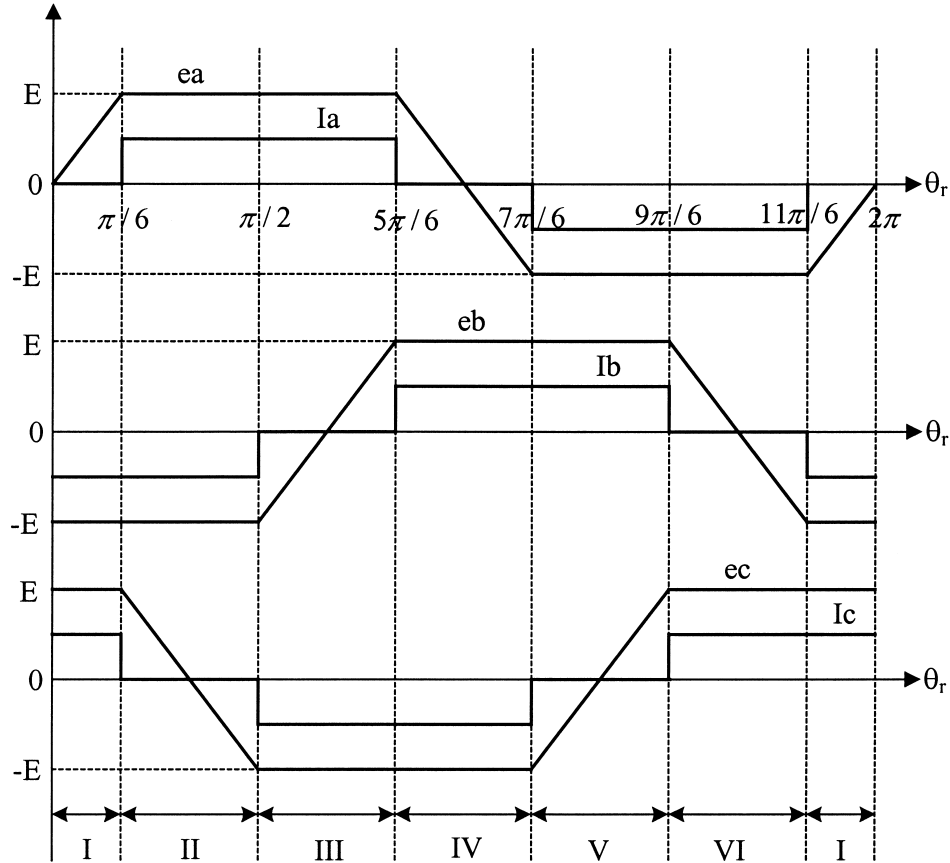
Figure 2. Back EMF and phase current waveforms of BLDC motor drive.
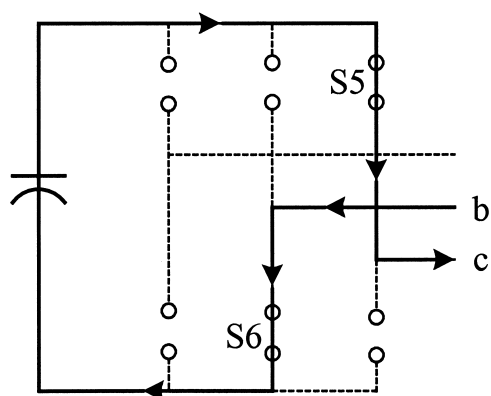
(a)
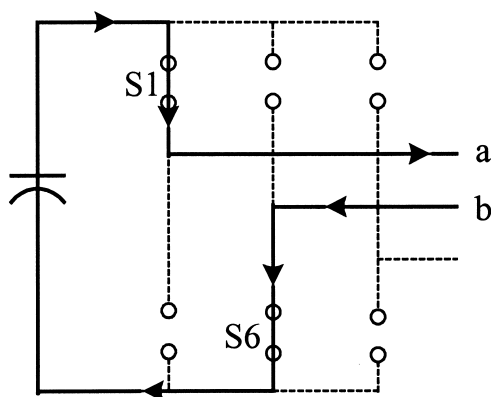
(b)
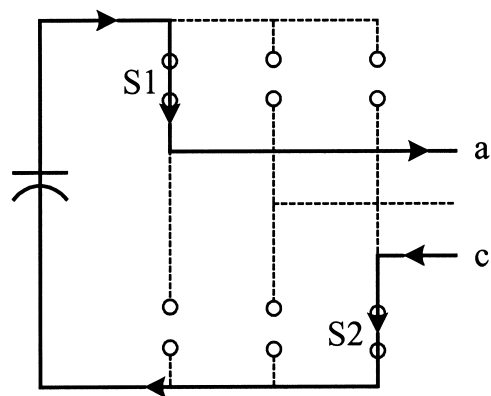
(c)

Figure 3. Switching states and conduction sequence according to the operating modes.
(a) Mode I ($I_a = 0, I_b < 0, I_c > 0$). (b) Mode II ($I_a > 0, I_b < 0, I_c = 0$). (c) Mode III
($I_a > 0, I_b = 0, I_c < 0$).
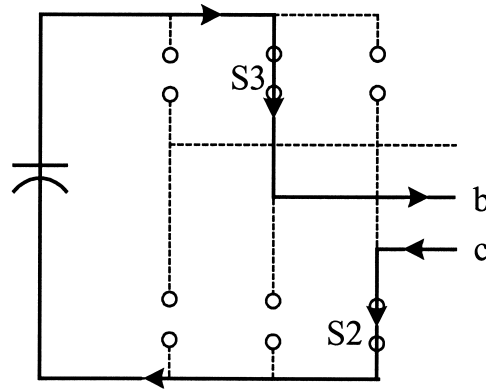
(d)
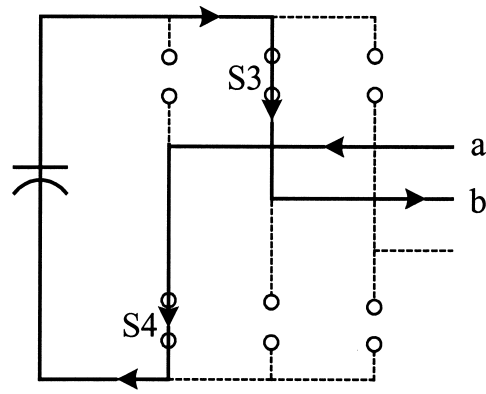
(e)
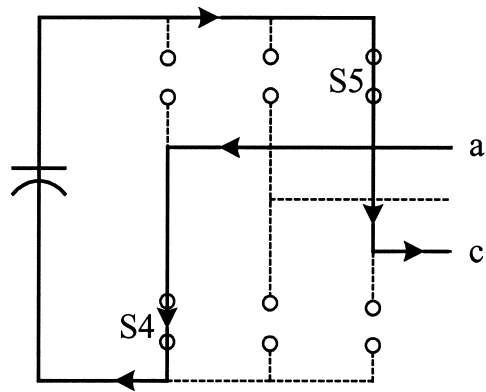
(f)

Figure 3. Switching states and conduction sequence according to the operating modes. (d) Mode IV ($I_a = 0, I_b > 0, I_c < 0$). (e) Mode V ($I_a < 0, I_b > 0, I_c = 0$). (f) Mode VI ($I_a < 0, I_b = 0, I_c > 0$).
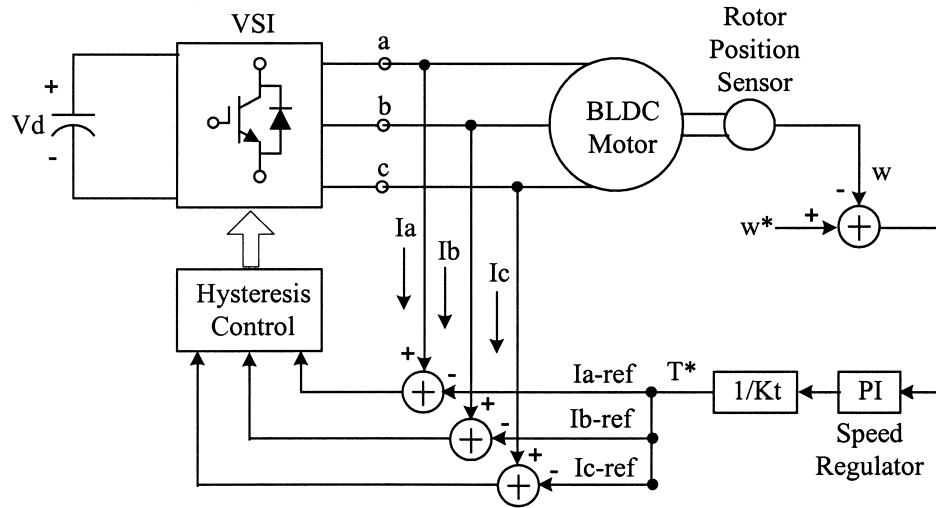
Figure 4. Block diagram of control scheme of BLDC motor drive.

3. Modeling and Implementation

In this section the modeling process is explained and the actual implementation using Matlab Simulink is described. Figure 5 shows the overall block diagram of the developed model for BLDC motor drives. As shown in Figure 5, the proposed model consists of seven functional blocks: back EMF block, load current block,
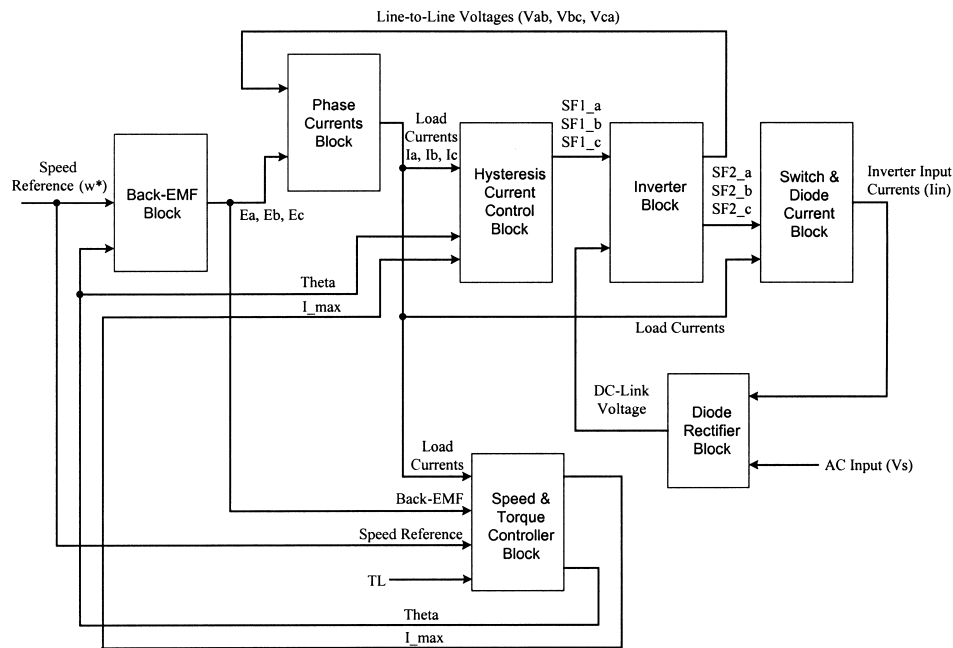
Figure 5. Overall block diagram of the developed model for BLDC motor drive systems.

hysteresis current control block, pwm inverter block, diode rectifier block, pure switch and diode current-generating block, and speed/torque controller block.

3.1. Back EMF Block

As shown in Figure 2, the back EMF is a function of rotor position (θ_r) and has the amplitude $E = K_e \cdot \omega_r$ (K_e is the back EMF constant). In this paper the modeling of the back EMF is performed under the assumption that all three phases have identical back EMF waveforms. Based on the rotor position, the numerical expression of the back EMF can be obtained as equations (3), (4), and (5), and it is implemented as shown in Figure 6. Therefore, with the speed command and rotor position, the symmetric three-phase back EMF waveforms can be generated at every operating speed:

$$e_a = \begin{cases} (6E/\pi)\theta_r & (0 < \theta_r < \pi/6) \\ E & (\pi/6 < \theta_r < 5\pi/6) \\ -(6E/\pi)\theta_r + 6E & (5\pi/6 < \theta_r < 7\pi/6), \\ -E & (7\pi/6 < \theta_r < 11\pi/6) \\ (6E/\pi)\theta_r - 12E & (11\pi/6 < \theta_r < 2\pi) \end{cases} \tag{3}$$

$$e_b = \begin{cases} -E & (0 < \theta_r < \pi/2) \\ (6E/\pi)\theta_r - 4E & (\pi/2 < \theta_r < 5\pi/6) \\ E & (5\pi/6 < \theta_r < 9\pi/6), \\ -(6E/\pi)\theta_r + 10E & (9\pi/6 < \theta_r < 11\pi/6) \\ E & (11\pi/6 < \theta_r < 2\pi) \end{cases} \tag{4}$$

$$e_c = \begin{cases} E & (0 < \theta_r < \pi/6) \\ -(6E/\pi)\theta_r + 2E & (\pi/6 < \theta_r < \pi/2) \\ -E & (\pi/2 < \theta_r < 7\pi/6). \\ (6E/\pi)\theta_r - 8E & (7\pi/6 < \theta_r < 9\pi/6) \\ E & (9\pi/6 < \theta_r < 2\pi) \end{cases} \tag{5}$$

In practical situations, due to manufacturing imperfection, deterioration of permanent magnets, or unbalanced stator windings, the back EMF waveforms become unbalanced. In this case the real back EMF could be modeled using finite element analysis (FEA). Consequently, the back EMF block can be modified by the FEA
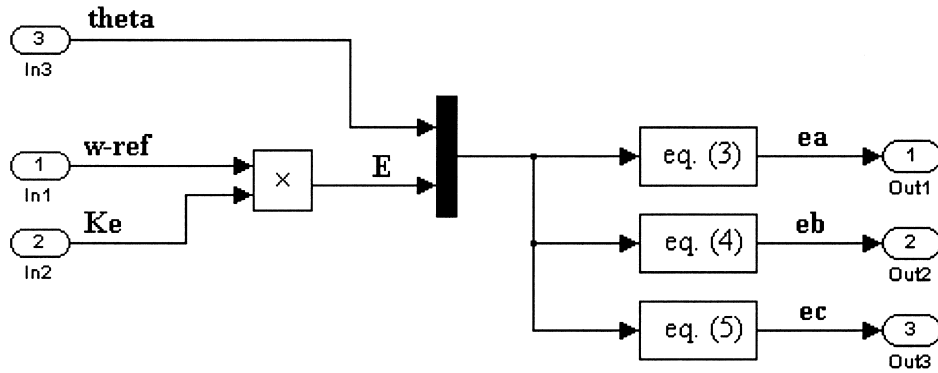

Figure 6. Back EMF generating block from rotor positions.

program. In the next step, these data will be fed into the "S-Function Block" in Matlab Simulink, which passes the program written in M, C, or Fortran to the Matlab workspace. Therefore, it is noted that the proposed model can be applied not only to the ideal back EMF case, but also to the practical case.

3.2. Speed and Torque Control Block

Speed and torque characteristics of the BLDC motor can be explained with equation (2), neglecting the damping factor as

$$\omega_r = \frac{1}{J}\int(T_e - T_L)dt = \frac{1}{J}\int[(T_a + T_b + T_c) - T_L]dt. \tag{6}$$

Therefore, the speed and torque control circuit can be implemented as shown in Figure 7.

3.3. Hysteresis Current Control Block

In the BLDC motor drive, duty-cycle controlled voltage pwm technique and hysteresis current control technique can be regarded as the main current control strategies. In this paper bipolar hysteresis current control is used for obtaining the fast dynamic responses during transient states. This current control method is explained based on the case of phase A. As shown in Figure 8 (a), current control for phase A can be divided into each four-period following the polarity of the current:

1. Case I: $I_a > 0$
   - Period 1: $I_a < Lower\ Limit\ (LL) \rightarrow$ Switch S_1 is turned on.
   - Period 2: $I_a > Upper\ Limit\ (UL) \rightarrow$ Switch S_1 is turned off and D_4 is conducted.
   - Period 3: $LL < I_a < UL$ and $dI_a/dt > 0 \rightarrow S_1$ is turned on.
   - Period 4: $LL < I_a < UL$ and $dI_a/dt < 0 \rightarrow$ Switch S_1 is turned off and D_4 is conducted.
2. Case II: $I_a < 0$
   - Period 1: $I_a > UL \rightarrow$ Switch S_4 is turned on.
   - Period 2: $I_a < LL \rightarrow$ Switch S_4 is turned off and D_1 is conducted.
   - Period 3: $LL < I_a < UL$ and $dI_a/dt < 0 \rightarrow S_4$ is turned on.
   - Period 4: $LL < I_a < UL$ and $dI_a/dt > 0 \rightarrow$ Switch S_4 is turned off and D_1 is conducted.

This hysteresis current control logic is realized in a function block $f_a(u)$ in cooperation with the measured phase A current I_a, current reference $I_{\max}$, and rotor position θ_r as shown in Figure 8 (b), such as

$$
\begin{aligned}
f_a(u) = {} & (u[4] > \pi/6) \cdot (u[4] < 5\pi/6) \\
& \cdot \begin{bmatrix} (u[1] < u[3] * 0.9) - (u[1] > u[3] * 1.1) \\ + (u[1] > u[3] * 0.9) * (u[1] < u[3] * 1.1) * (u[1] > u[2]) \\ - (u[1] > u[3] * 0.9) * (u[1] < u[3] * 1.1) * (u[1] < u[2]) \end{bmatrix} \\
& + (u[4] > 7\pi/6) \cdot (u[4] < 11\pi/6) \\
& \cdot \begin{bmatrix} -(u[1] > -u[3] * 0.9) + (u[1] < -u[3] * 1.1) \\ - (u[1] < -u[3] * 0.9) * (u[1] > -u[3] * 1.1) * (u[1] < u[2]) \\ + (u[1] < -u[3] * 0.9) * (u[1] > -u[3] * 1.1) * (u[1] > u[2]) \end{bmatrix},
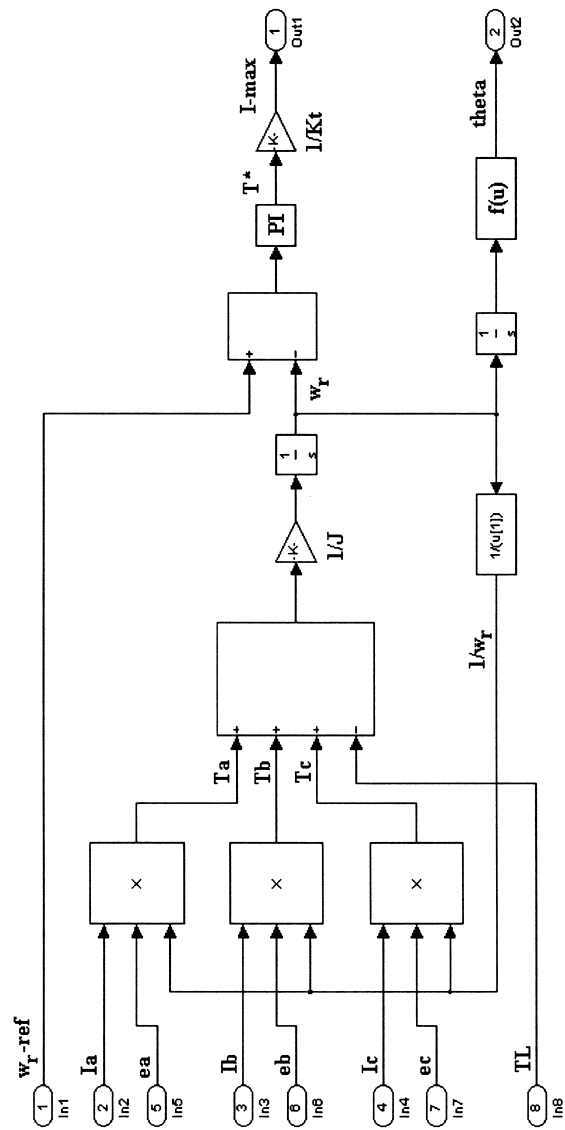\end{aligned}
\tag{7}
$$

Figure 7. Speed and torque control block.
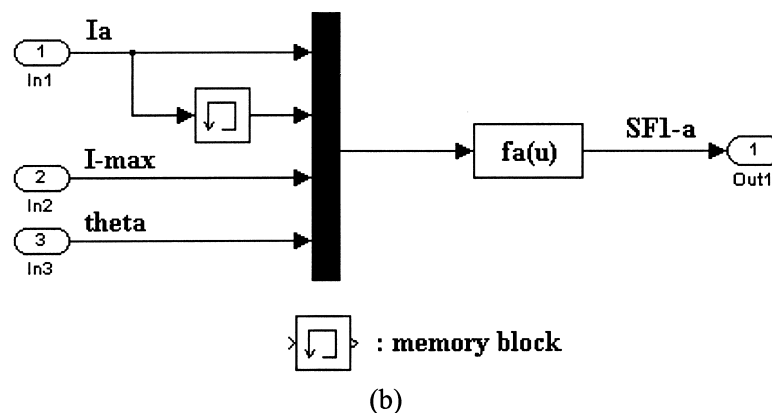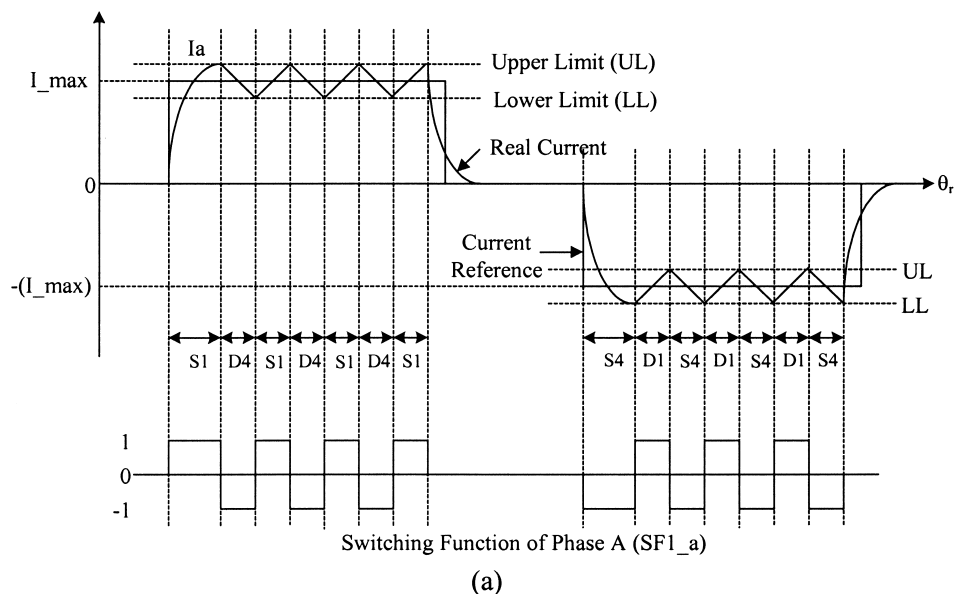
Figure 8. (a) Detailed investigation of hysteresis current control for phase A, and (b) its implementation.

where $u[1]$ is the measured I_a, $u[2]$ is the previous value of I_a, $u[3]$ is the maximum value of current reference ($I_{-\max}$), $u[4]$ is the rotor position (θ_r), $u[3]*0.9$ is the lower limit, and $u[3]*1.1$ is the upper limit.

From the hysteresis block, the switching function SF_{1_a}, SF_{1_b}, and SF_{1_c} are determined to model the operation of the pwm inverter. The switching function concept is a powerful tool in understanding and optimizing the performance of the static power converters/inverters [13–17]. Using the switching function concept, the power conversion circuits can be modeled according to their functions, rather than circuit topologies. Therefore, it can achieve simplification of the overall power

conversion functions, so that the convergence and long-run time problems, which are common in PSPICE and SABER, can be solved [17].

In this model the switching function SF_1 is used to generate the inverter line-to-line voltages. Also, it is modified to SF_2 for obtaining the pure switch and diode currents according to the switching states. Consequently, using switching functions (SF_1 and SF_2), the detailed inverter operation under hysteresis current control can be effectively expressed.

3.4. PWM Inverter, Load Current, and Pure Switch/Diode Current Blocks

As shown in Figure 3, only the two phases are excited through the conduction operating modes. Therefore, the three-phase currents are considered in terms of the line-to-line voltages. From Figure 9, the following voltage and current equations can be obtained:

$$\left[\begin{aligned} v_{ab} &= R_{LL}i_1 + (L-M)_{LL}\frac{di_1}{dt} + e_{ab}, \\ v_{bc} &= R_{LL}i_2 + (L-M)_{LL}\frac{di_2}{dt} + e_{bc}, \\ v_{ca} &= R_{LL}i_3 + (L-M)_{LL}\frac{di_3}{dt} + e_{ca}, \end{aligned} \right. \tag{8}$$

where

R_{LL} is the line-to-line resistance and equals $2R$
$(L-M)_{LL}$ is the line-to-line inductance and equals $2(L-M)$
e_{ab}, e_{bc}, and e_{ca} are the line-to-line back EMFs, $e_{ab} = e_a - e_b$, $e_{bc} = e_b - e_c$, $e_{ca} = e_c - e_a$
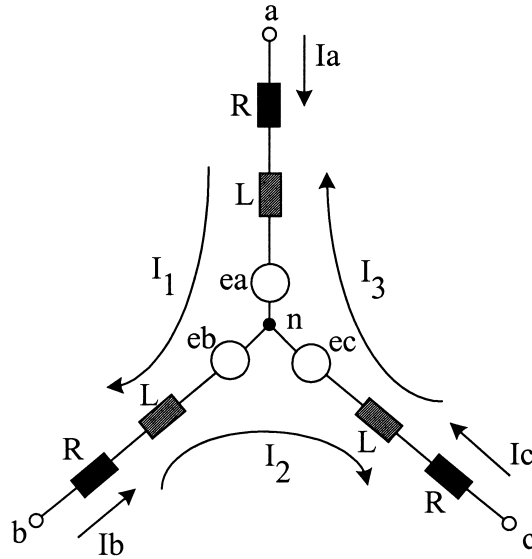

Figure 9. Voltage and current parameters in three-phase BLDC motor.

and

$$\begin{cases} i_a = i_1 - i_3, \\ i_b = i_2 - i_1, \\ i_c = i_3 - i_2. \end{cases} \tag{9}$$

Using switching function $\mathrm{SF}_{1\_a,b,c}$, which is obtained from hysteresis block, v_{ao}, v_{bo}, and v_{co} can be calculated as

$$\begin{cases} v_{ao} = \dfrac{V_d}{2}\mathrm{SF}_{1\_a} = \dfrac{V_d}{2}\sum_{0}^{\infty} A_n \sin(n\omega t), \\[2ex] v_{bo} = \dfrac{V_d}{2}\mathrm{SF}_{1\_b} = \dfrac{V_d}{2}\sum_{0}^{\infty} A_n \sin n(\omega t - 120°), \\[2ex] v_{co} = \dfrac{V_d}{2}\mathrm{SF}_{1\_c} = \dfrac{V_d}{2}\sum_{0}^{\infty} A_n \sin n(\omega t - 240°). \end{cases} \tag{10}$$

Then the inverter line-to-line voltages can be derived as

$$\begin{cases} v_{ab} = v_{ao} - v_{bo} = \dfrac{V_d}{2}(\mathrm{SF}_{1\_a} - \mathrm{SF}_{1\_b}), \\[2ex] v_{bc} = v_{bo} - v_{co} = \dfrac{V_d}{2}(\mathrm{SF}_{1\_b} - \mathrm{SF}_{1\_c}), \\[2ex] v_{ca} = v_{co} - v_{ao} = \dfrac{V_d}{2}(\mathrm{SF}_{1\_c} - \mathrm{SF}_{1\_a}). \end{cases} \tag{11}$$

Next, the three-phase currents are obtained solving equations (8) and (9). From the calculated phase currents, the detailed pure switch and diode currents are derived using switching function SF_2. Each phase has two switching functions of SF_2, such as SF_{2_S1} and SF_{2_S4} for switches S_1 and S_4, respectively, with the following definition:

$$\begin{cases} \mathrm{SF}_{2\_S1} = \mathrm{SF}_{1\_a} > 0, \\ \mathrm{SF}_{2\_S4} = \mathrm{SF}_{1\_a} < 0. \end{cases} \tag{12}$$

Based on equation (12) and Figure 8 (a), the switch and diode currents for phase A are calculated as

$$\begin{cases} I_{\mathrm{S1\_S}} = (I_a > 0) \cdot \mathrm{SF}_{2\_S1}, \\ I_{\mathrm{S1\_D}} = (I_a < 0) \cdot \mathrm{SF}_{2\_S1}, \\ I_{\mathrm{S4\_S}} = (I_a < 0) \cdot \mathrm{SF}_{2\_S4}, \\ I_{\mathrm{S1\_D}} = (I_a > 0) \cdot \mathrm{SF}_{2\_S4}, \end{cases} \tag{13}$$

where

$I_{\mathrm{S1\_S}}$ and $I_{\mathrm{S1\_D}}$ are pure switch and diode currents of switch S_1 as $I_{\mathrm{S1}} = I_{\mathrm{S1\_S}} - I_{\mathrm{S1\_D}}$ $I_{\mathrm{S4\_S}}$ and $I_{\mathrm{S4\_D}}$ are pure switch and diode currents of switch S_4 as $I_{\mathrm{S4}} = I_{\mathrm{S4\_S}} - I_{\mathrm{S4\_D}}$.

Also, the inverter input current (I_{in}) can be obtained by

$$I_{in} = L_{\mathrm{S1}} + I_{\mathrm{S3}} + L_{\mathrm{S5}}. \tag{14}$$

Finally, the average and rms values of current parameters can be expressed by the vector forms such as equations (15) and (16) and can be calculated in the Matlab workspace by getting the data from Figure 5:

$$I_{\text{S1\_S},avg} = \frac{1}{T}\int_0^T I_{\text{S1\_S}}(t)dt = \frac{1}{2n}\sum_{k=1}^n [I_{\text{S1\_S}}(k) + I_{\text{S1\_S}}(k-1)], \tag{15}$$

$$I_{\text{S1\_S},rms} = \sqrt{\frac{1}{T}\int_0^T I_{\text{S1\_S}}^2(t)dt} = \sqrt{\frac{1}{2n}\sum_{k=1}^n [I_{\text{S1\_S}}^2(k) + I_{\text{S1\_S}}^2(k-1)]}. \tag{16}$$

The implementations of the above-explained numerical pwm inverter voltage and current equations are shown in Figures 10, 11, and 12. Consequently, from the inverter, load current, and switch/diode blocks, all voltage and current variables of the pwm inverter can be obtained.

4. Simulation Results

Table 1 shows the BLDC motor specification to examine the performance of the proposed model. Figure 13 shows the generated back EMF from the rotor position and the phase-current waveforms according to each operating speed, such as 2,500 and 3,500 rpm. As shown in Figure 13, the three-phase symmetric back EMF waveforms are actively calculated and generated from the rotor position. At 2,500 rpm,
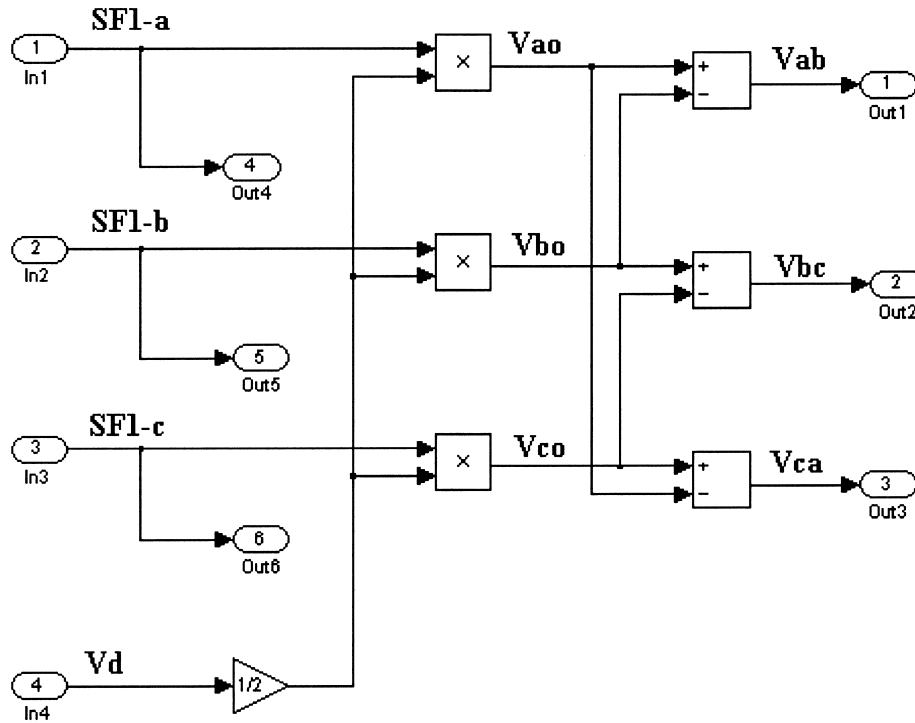

Figure 10. Inverter line-to-line voltage-generating block using switching functions.
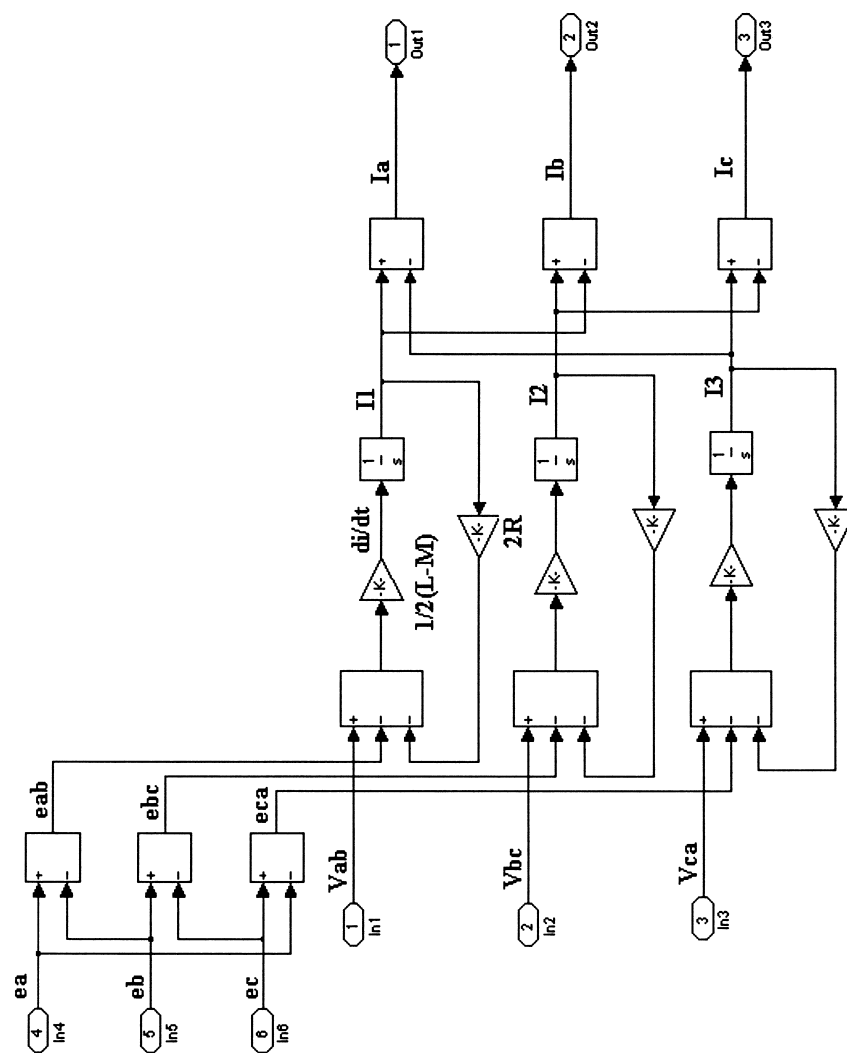
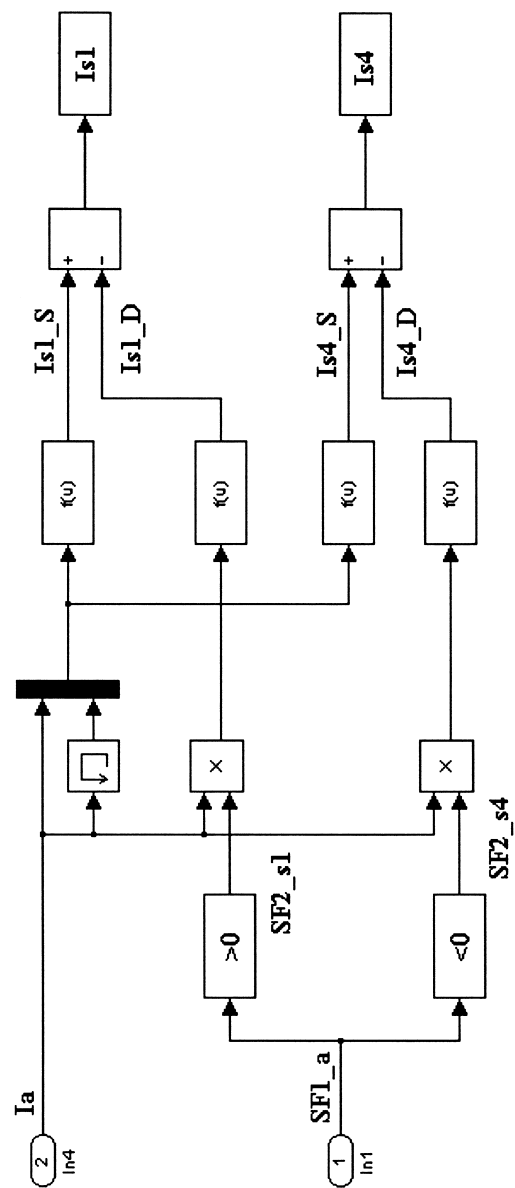Figure 11. Implementation of three-phase currents block.

854

Figure 12. Pure switch and diode currents-generating block for phase A.

Table 1

Motor specification (LL: line-to-line)

K_t	0.21476 Nm	$R_{\_LL}$	1.5 Ω
K_{e_LL}	0.21486 V/(rad/sec)	$(L\text{-}M)_{\_LL}$	6.1 mH
J	8.2614e − 5 kgm^2	Power	1 HP
T_L	0.662 Nm	Rated speed	3,500 rpm

the rotor position is varied from 0 to 2π per electric cycle 0.024 s, and the back EMF has an amplitude of 28.11 V. On the other hand, at 3,500 rpm, the electric cycle is 0.017 s, and the amplitude is 39.36 V. Also, the actual phase currents are successfully obtained by the hysteresis control algorithm, and they are well synchronized with their counterpart back EMF waveforms as explained above. In Figure 14, the expanded current waveforms for phase A are depicted. In these waveforms, the current pulsation is measured at the middle of 120° conduction periods. They result from the commutation of the other two phases (phases B and C).

The detailed analysis of the torque ripple due to the commutation is well explained in [10]. Based on the simulation conditions at 3,500 rpm, DC-link voltage (160 V) is larger than the value of $4E$ (157.44 V), that is, $V_d > 4E$. Therefore, the phase C current reaches the $I_{\max}$ value before phase B current goes to zero [10]. As the result, the phase A current decreases, and torque increases during the commutation period. This phenomenon can be observed in Figure 15. Therefore, it is noted that in the developed simulation model, the transient characteristics are well examined as well as the steady-state ones.

Figure 16 (a) shows the dynamic responses of the speed and torque controller, which is designed as shown in Figure 7. With the help of the PI controller, the real speed reaches the command value in 0.02 s. Also, from the generated constant torque reference, the maximum current reference value ($I_{\max}$) is calculated, and then it is used in the hysteresis control block. From the expanded waveform in Figure 16 (b), the torque pulsation due to the commutation can be measured, and using equation (15), the average values of torque and the maximum current reference value are calculated as about 0.65 Nm and 3.15 A, respectively.

From Figures 17 and 18, the detailed operational characteristics of the pwm inverter are examined. As explained above, the pwm inverter modeling is based on the switching function concept. Figures 17 (a) and (b) show the switching function SF_1 for the three phases (SF_{1_a}, SF_{1_b}, SF_{1_c}). From the figures, it is noted that the switching function signals are generated only during the 120° conduction periods in order to force the currents to be switched between the hysteresis upper and lower bands. The positive (negative) value 1 (-1) expresses that the upper (lower) switch or diode is under the conducting state. Therefore, from the switching function SF_1, the line-to-line voltage waveforms can be obtained. Figures 17 (c) and (d) show the generated line-to-line voltage (V_{ab}) according to the conduction modes. In case of Figure 17 (c), the phase A current is positive and the phase B current is negative, which is mode II in Figure 3. Therefore, during the positive slope of phase A ($di_a/dt > 0$) and negative slope of phase B ($di_b/dt < 0$), switches S_1 and S_6 are conducted, so that V_{ab} has a positive value of V_d (160 V). On the other hand, V_{ab} has negative V_d for the period $di_a/dt < 0$ and $di_b/dt > 0$ (diodes D_4 and D_3 are conducted).
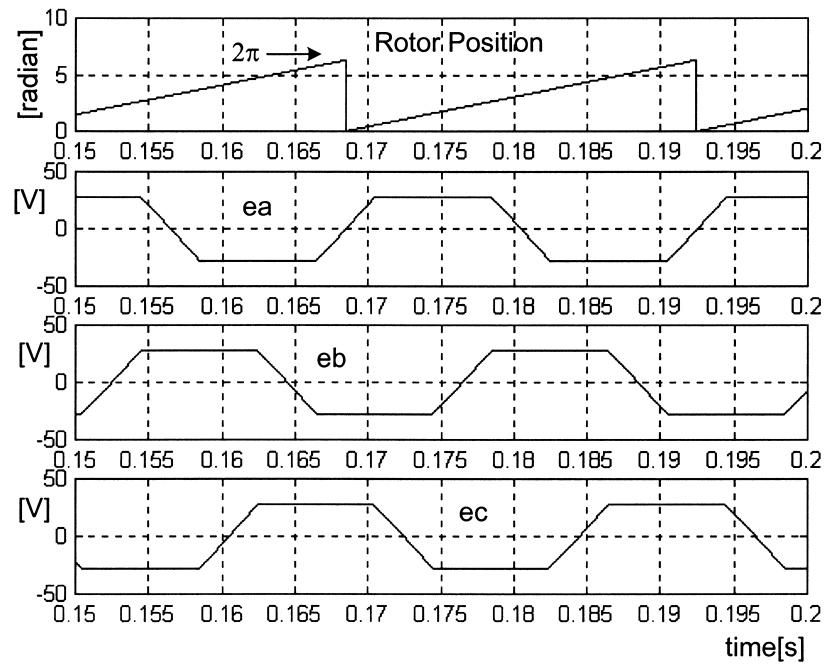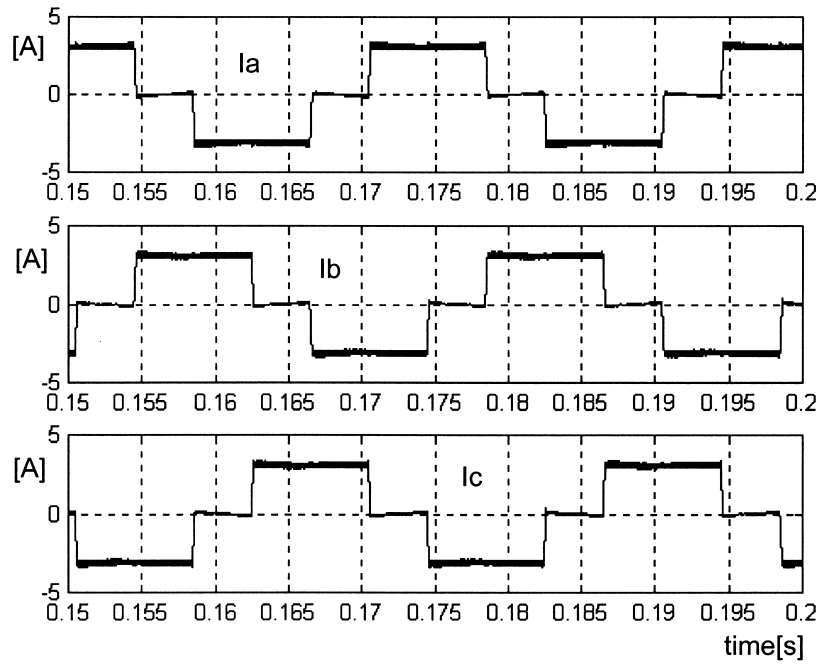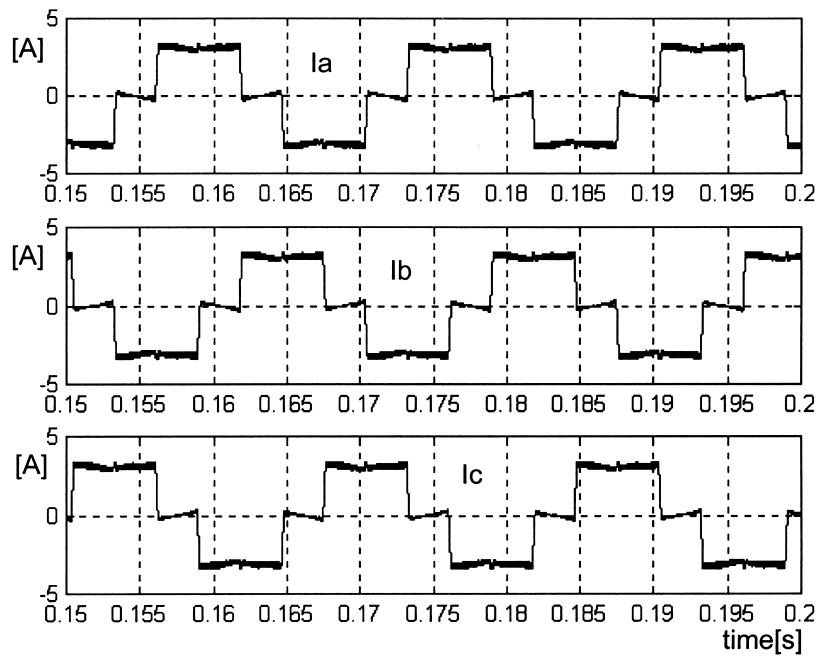
(a)
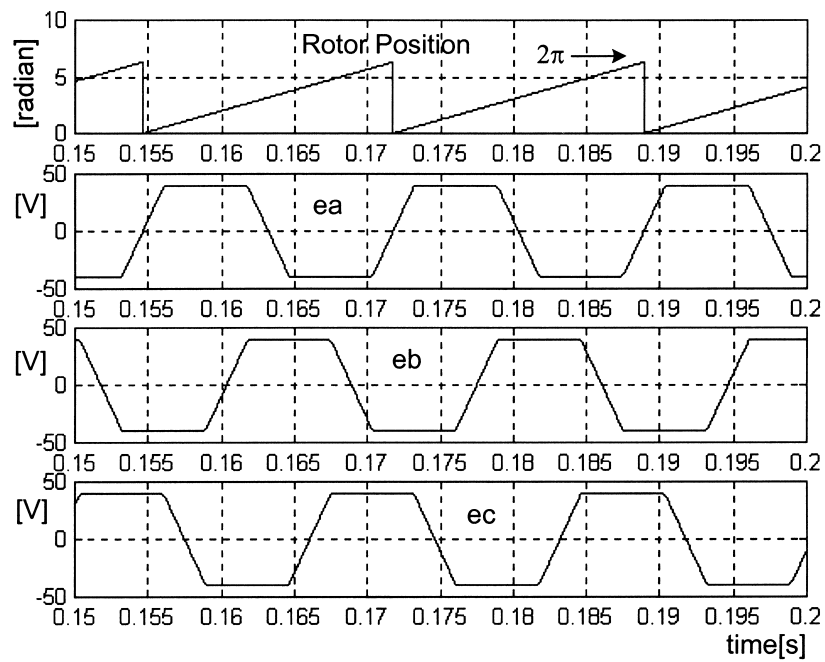
(b)

Figure 13. Back EMF (upper) and phase currents (lower) waveforms based on the rotor position. (a) At 2,500 rpm. (b) At 3,500 rpm.
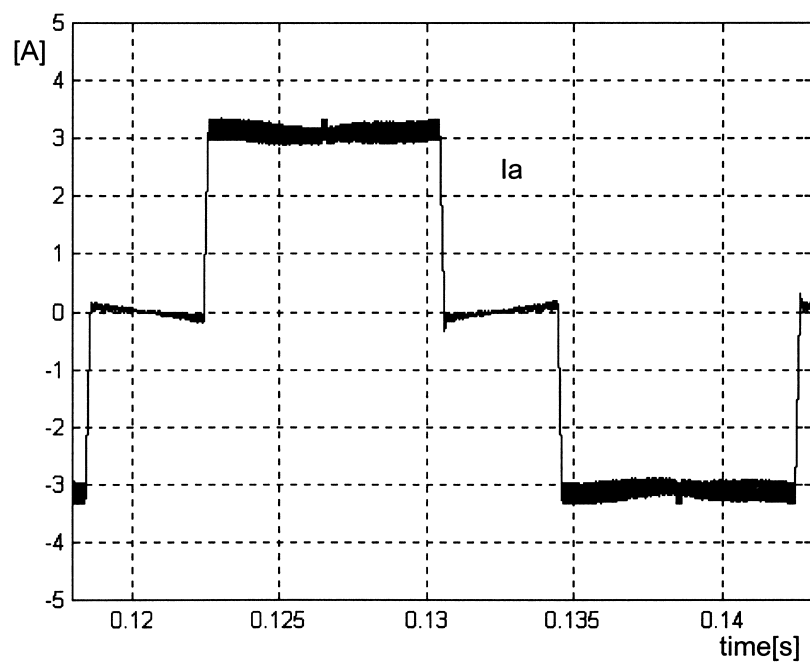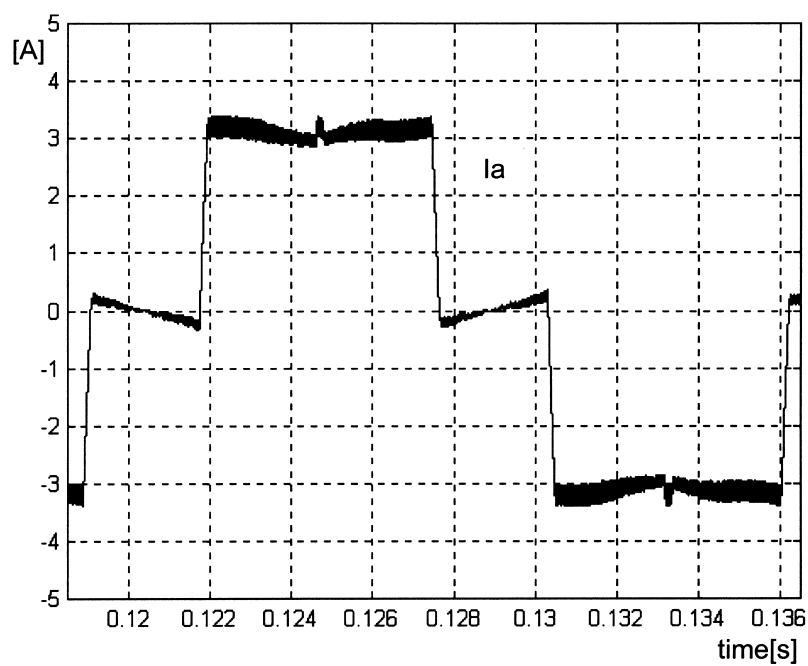
(c)

(d)

Figure 13. Back EMF (upper) and phase currents (lower) waveforms based on the rotor position. (c) At 2,500 rpm. (d) At 3,500 rpm.
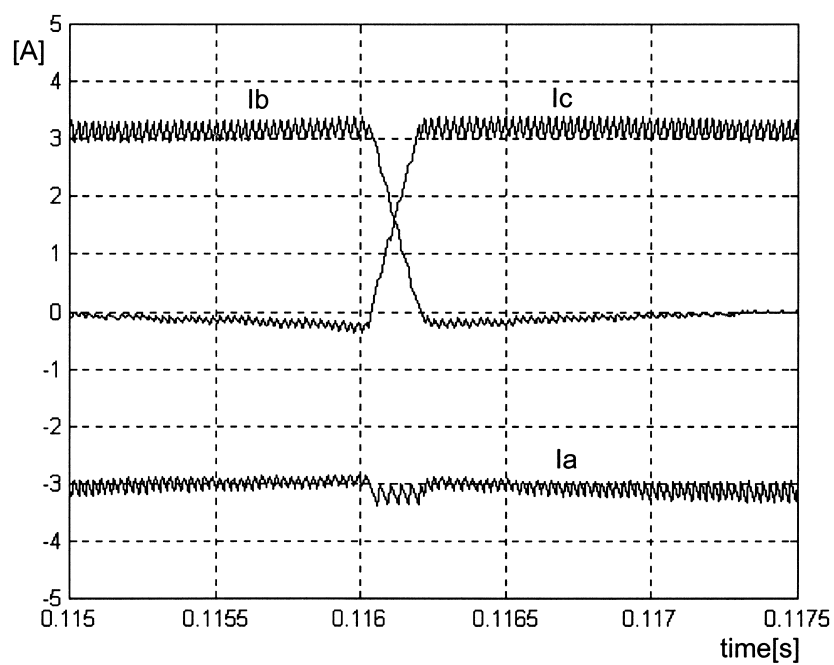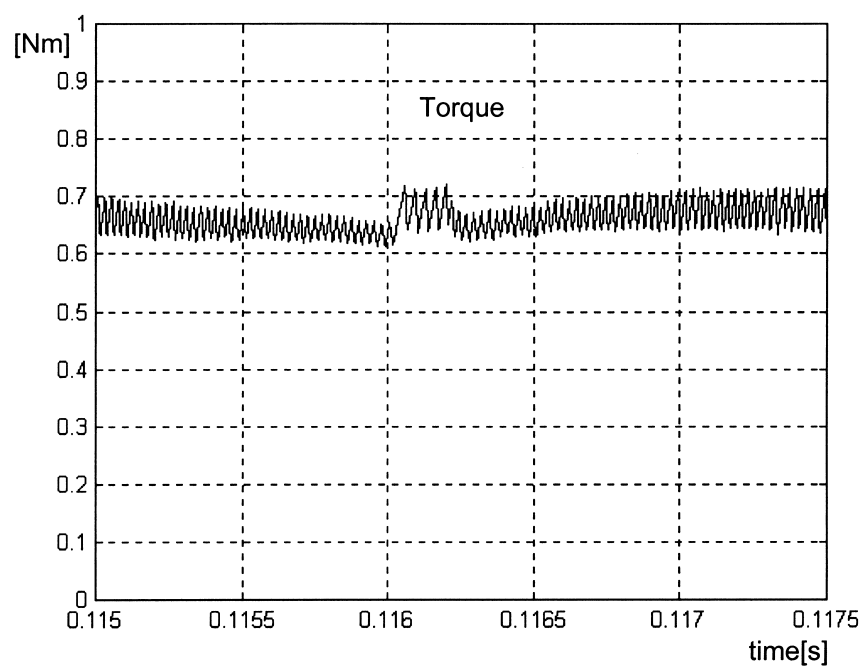
(a)

(b)

Figure 14. Expanded current waveforms for phase A. (a) At 2,500 rpm. (b) At 3,500 rpm.

(a)

(b)

Figure 15. Phase current and torque pulsations during the commutation period at 3,500 rpm. (a) Phase currents. (b) Torque.
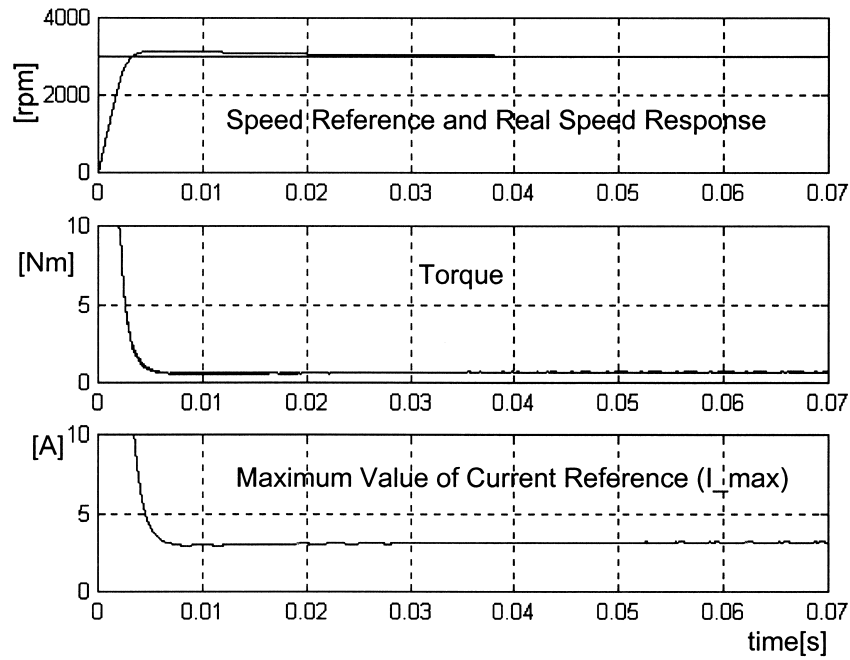
(a)
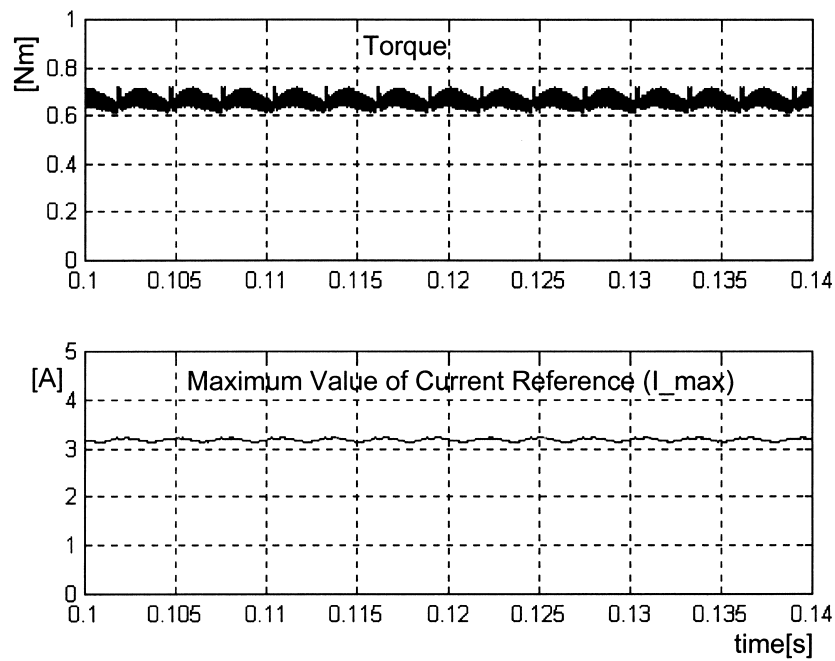
(b)

Figure 16. (a) Dynamic responses of speed and torque controller. (b) Expanded waveforms.
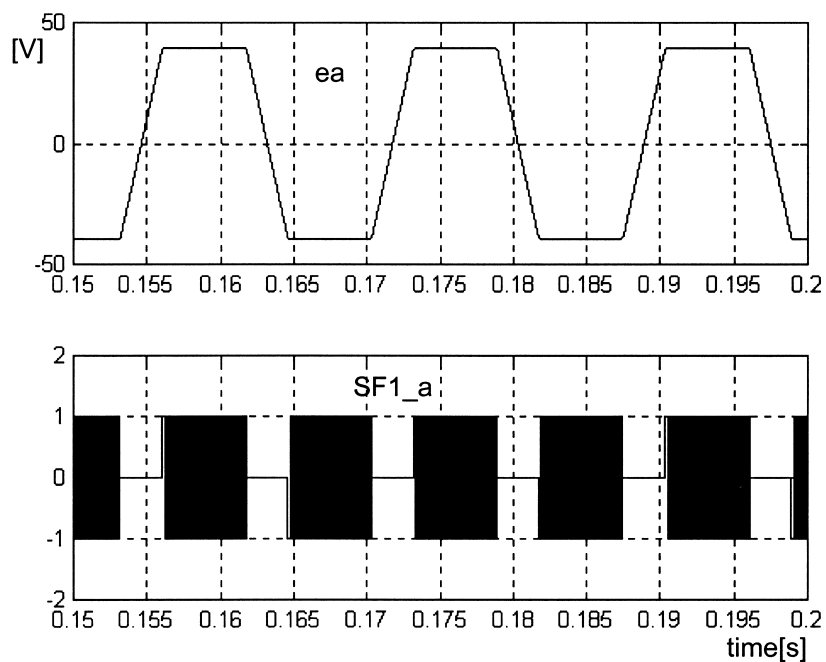
(a)
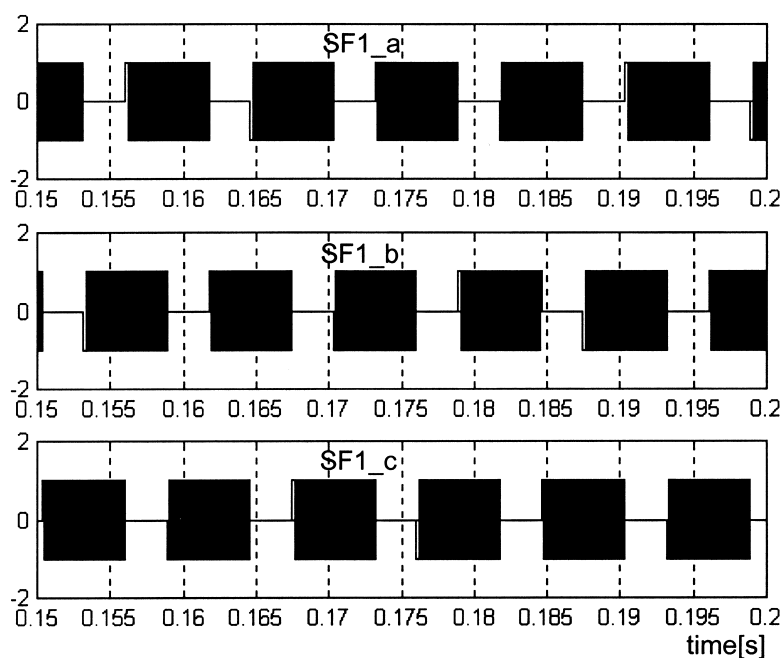
(b)

Figure 17. Switching function $SF_{1\text{-}a,b,c}$ and line-to-line voltage (V_{ab}) waveforms according to the conducting modes. (a) Back EMF and switching function for phase A. (b) Switching function SF_1.
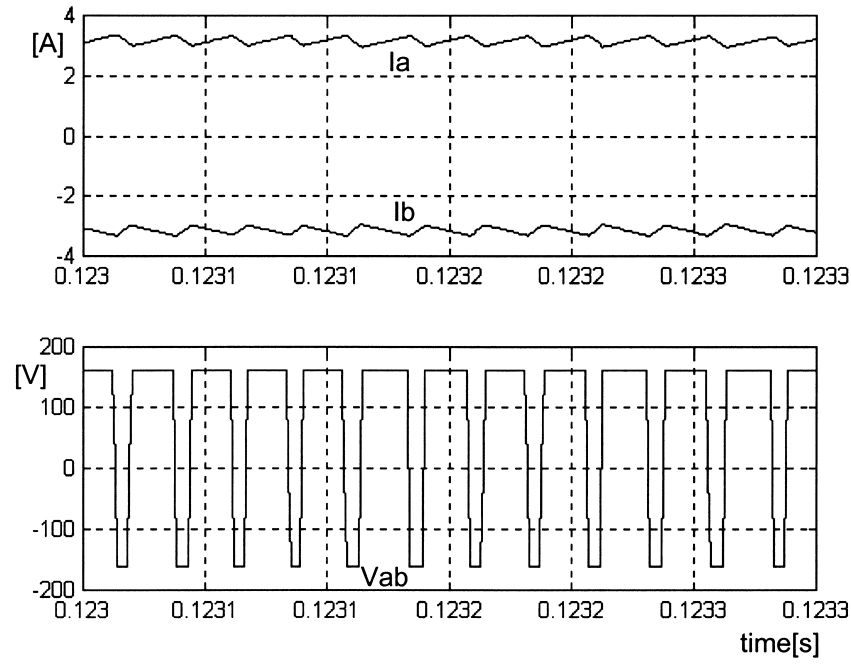
(c)
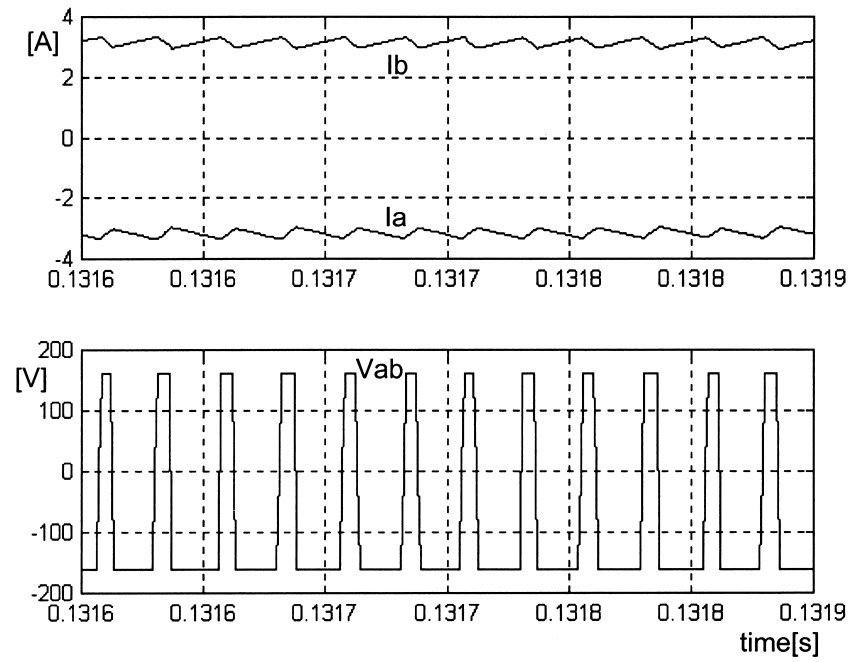
(d)

Figure 17. Switching function $SF_{1\_a,b,c}$ and line-to-line voltage (V_{ab}) waveforms according to the conducting modes. (c) Line-to-line voltage $V_{ab}(I_a > 0, I_b < 0)$. (d) Line-to-line voltage $V_{ab}(I_a < 0, I_b > 0)$.
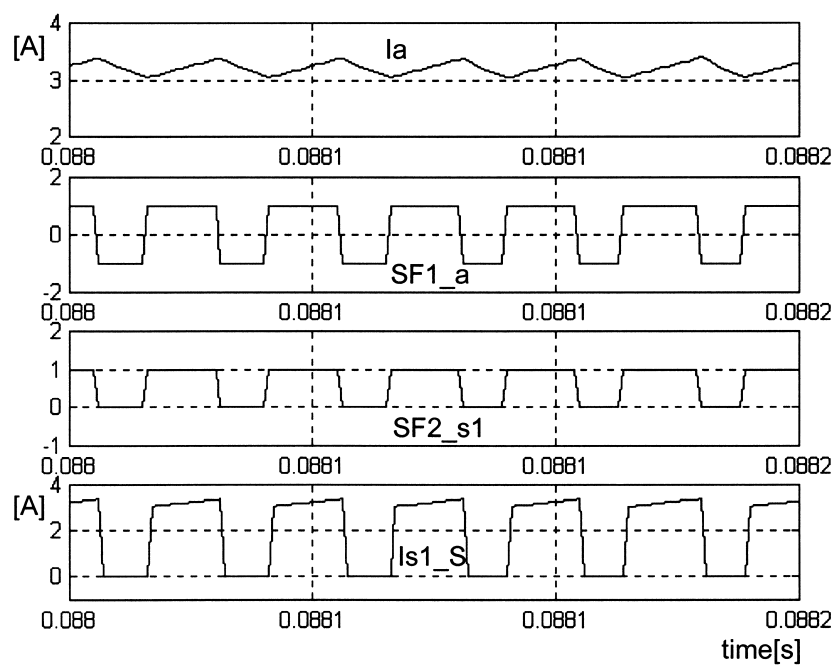
(a)
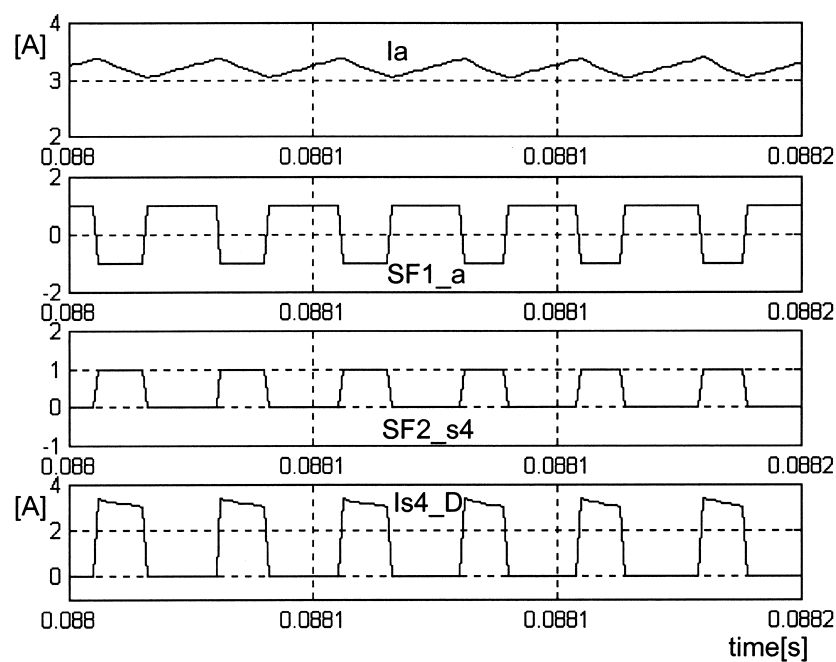
(b)

Figure 18. Pure switch and diode current waveforms of switch S_1. (a) Pure switch current I_{s1_S} $(I_a > 0)$. (b) Pure diode currents I_{s4_D} $(I_a > 0)$.
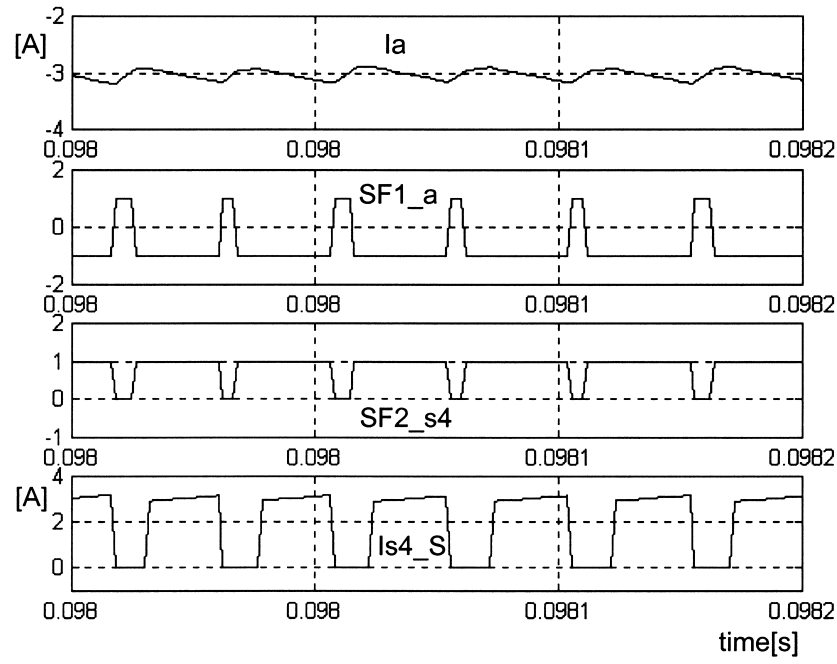
(c)
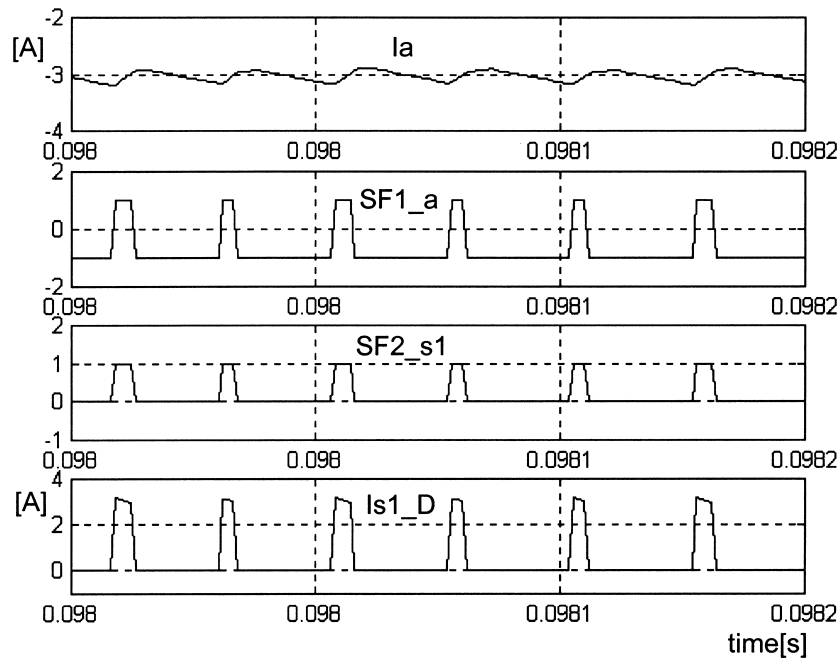
(d)

Figure 18. Pure switch and diode current waveforms of switch S_1. (c) Pure switch current I_{s4_S} ($I_a < 0$). (d) Pure diode currents I_{s1_D} ($I_a < 0$).

A similar explanation can be applied to the case of $I_a < 0$ and $I_b > 0$ (mode V), as shown in Figure 17 (d). Consequently, the patterns of the line-to-line voltages (V_{ab}, V_{bc}, V_{ca}) and conducting devices according to the current states are summarized in Tables 2–4.

In order to obtain the optimal design parameters of the pwm inverter, the pure switch and diode current waveforms are necessary for calculating the average and

Table 2
V_{ab} and conducting devices according to the current states

|			I_a			
			>0		<0	
V_{ab} and conducting devices			$di_a/dt > 0$	$di_a/dt < 0$	$di_a/dt > 0$	$di_a/dt < 0$
I_b	>0	$di_b/dt > 0$	×	×	×	$-V_d, S_3, S_4$
		$di_b/dt < 0$	×	×	V_d, D_1, D_6	×
	<0	$di_b/dt > 0$	×	$-V_d, D_3, D_4$	×	×
		$di_b/dt < 0$	V_d, S_1, S_6	×	×	×

Table 3
V_{bc} and conducting devices according to the current states

			I_b			
			>0		<0	
V_{bc} and conducting devices			$di_b/dt > 0$	$di_b/dt < 0$	$di_b/dt > 0$	$di_b/dt < 0$
I_c	>0	$di_c/dt > 0$	×	×	×	$-V_d, S_5, S_6$
		$di_c/dt < 0$	×	×	V_d, D_2, D_3	×
	<0	$di_c/dt > 0$	×	$-V_d, D_5, D_6$	×	×
		$di_c/dt < 0$	V_d, S_2, S_3	×	×	×

Table 4
V_{ca} and conducting devices according to the current states

			I_c			
			>0		<0	
V_{ca} and conducting devices			$di_c/dt > 0$	$di_c/dt < 0$	$di_c/dt > 0$	$di_c/dt < 0$
I_a	>0	$di_a/dt > 0$	×	×	×	$-V_d, S_1, S_2$
		$di_a/dt < 0$	×	×	V_d, D_4, D_5	×
	<0	$di_a/dt > 0$	×	$-V_d, D_1, D_2$	×	×
		$di_a/dt < 0$	V_d, S_4, S_5	×	×	×

rms values. They also can be obtained from the combination of the phase currents and switching function SF_2. Figure 18 explains the detailed process of calculating the pure switch and diode currents.

In case of $I_a > 0$, the current can be flowing through the switch S_1 or diode D_4. If the current is increased ($d_{ia}/dt > 0$), the switch S_1 is turned on, and the current flows through switch S_1. Also, when the current is decreased ($d_{ia}/dt > 0$), the switch S_1 is turned off, and the current is conducted through the diode D_4. The switching function SF_2 for S_1 (SF_{2_S1}) and D_4 (SF_{2_S4}) are obtained from the switching function SF_{1_a}, which is explained in equation (12). As the result, the pure switch and diode currents can be successfully obtained. As shown in Figures 18 (a) and (b), the only positive slope part of phase current I_a is selected as the pure switch current I_{s1_S}, and the negative slope part is as the pure diode current I_{s4_D}. In case of $I_a < 0$, the switch S_4 and the diode D_1 provide the current path, and the pure switch current I_{s4_S} and the pure diode current I_{s1_D} can be expressed as shown in Figure 18 (d).

After obtaining the pure switch and diode current waveforms, the average and rms values can be easily calculated using equations (15) and (16). As an example, for S_1 and D_1, the average values are calculated as 0.657 and 0.240 A, respectively, under an operating speed of 3,500 rpm, and the hysteresis window size is 10% of the maximum current reference values. Also, for rms values, one can obtain 1.415 and 0.871 A.

5. Conclusions

In this paper an advanced simulation model for BLDC motor drives is proposed, and the performance and feasibilities have been examined by the informative simulation verification. From the investigation of the developed simulation model, it is expected that the dynamic characteristics as well as the steady state can be effectively monitored and predicted, so that the performance of a developed system can be more precisely analyzed according to the variation of the control algorithm and topology.

References

[1] A. Kusko and S. M. Peeran, "Definition of the brushless DC motor," *Proc. of the IEEE Industry Application Society Annual Meeting IAS'88*, pp. 20–22, 1988.

[2] J. R. Hendershot and T. J. E. Miller, *Design of Brushless Permanent-Magnet Motor*, Oxford: Oxford Science, 1994.

[3] T. Kenjo and S. Nagamori, *Permanent Magnet and Brushless DC Motors*, Tokyo: Sogo Electronics, 1984.

[4] D. C. Hanselman, *Brushless Permanent-Magnet Motor Design*, New York: McGraw-Hill, 1994.

[5] T. M. Jahns, "Motion control with permanent-magnet AC machines," *Proc. of the IEEE*, vol. 82, no. 8, pp. 1241–1252, 1994.

[6] T. A. Lipo and F. G. Turnbull, "Analysis and comparison of two types of square-wave inverter drives," *IEEE Trans. on Industry Applications*, vol. 11, no. 2, pp. 137–147, March/April 1975.

[7] T. M. Jahns and W. L. Soong, "Pulsating torque minimization techniques for permanent magnet AC motor drives—a review," *IEEE Trans. on Industry Applications*, vol. 43, no. 2, pp. 321–330, April 1996.

[8] J. P. Johnson and M. Ehsani, "Review of sensorless methods for brushless DC," *Proc. of the IEEE Industry Application Society Annual Meeting IAS'99*, pp. 143–150, 1999.

[9] P. Pillay and R. Krishnan, "Modeling, simulation, and analysis of permanent-magnet motor drives, part II: the brushless DC motor drive," *IEEE Trans. on Industry Applications*, vol. 25, no. 2, pp. 274–279, March/April 1989.

[10] R. Carlson, M. Lajoie-Mazenc, and C. dos S. Fagundes, "Analysis of torque ripple due to phase commutation in brushless DC machines," *IEEE Trans. on Industry Applications*, vol. 28, no. 3, pp. 632–638, May/June 1992.

[11] P. D. Evans and D. Brown, "Simulation of brushless DC drives," *Proc. of the IEE*, vol. 137, no. 5, pp. 299–308, September 1990.

[12] S. K. Safi, P. P. Acarnley, and A. G. Jack, "Analysis and simulation of the high-speed torque performance of brushless DC motor drives," *Proc. of the IEE*, vol. 142, no. 3, pp. 191–200, May 1995.

[13] P. Wood, *Theory of Switching Power Converter*, New York: Van Nostrand-Reinhold, 1981.

[14] P. D. Ziogas, E. P. Wiechmann, and V. R. Stefanovic, "A computer-aided analysis and design approach for static voltage source inverter," *IEEE Trans. on Industry Applications*, vol. IA-21, no. 5, pp. 1234–1241, September/October 1985.

[15] E. P. Wiechmann, P. D. Ziogas, and V. R. Stefanovic, "Generalized functional model for three phase PWM inverter/rectifier converters," *Proc. of the IEEE Industry Application Society Annual Meeting IAS'85*, pp. 984–993, 1985.

[16] L. Salazar and G. Joos, "PSPICE simulation of three-phase inverters by means of switching functions," *IEEE Trans. on Power Electronics*, vol. 9, no. 1, pp. 35–42, January 1994.

[17] B. K. Lee and M. Ehsani, "A simplified functional model for 3-phase voltage-source inverter using switching function concept," *IEEE Trans. on Industrial Electronics*, vol. 48, no. 2, pp. 309–321, April 2001.